Clim Dyn (2016) 46:2179–2196
DOI 10.1007/s00382-015-2696-9

A case study of effects of atmospheric boundary layer turbulence, wind speed, and stability on wind farm induced temperature changes using observations from a field campaign

Geng Xia[1] · Liming Zhou[1] · Jeffrey M. Freedman[2] · Somnath Baidya Roy[3] · Ronald A. Harris[1] · Matthew Charles Cervarich[4]

Received: 4 December 2014 / Accepted: 30 May 2015 / Published online: 12 June 2015

Abstract Recent studies using satellite observations show that operational wind farms in west-central Texas increase local nighttime land surface temperature (LST) by 0.31–0.70 °C, but no noticeable impact is detected during daytime, and that the diurnal and seasonal variations in the magnitude of this warming are likely determined by those in the magnitude of wind speed. This paper further explores these findings by using the data from a year-long field campaign and nearby radiosonde observations to investigate how thermodynamic profiles and surface–atmosphere exchange processes work in tandem with the presence of wind farms to affect the local climate. Combined with satellite data analyses, we find that wind farm impacts on LST are predominantly determined by the relative ratio of turbulence kinetic energy (TKE) induced by the wind turbines compared to the background TKE. This ratio explains not only the day–night contrast of the wind farm impact and the warming magnitude of nighttime LST over the wind farms, but also most of the seasonal variations in the nighttime LST changes. These results indicate that the diurnal and seasonal variations in the turbine-induced turbulence relative to the background TKE play an essential role in determining those in the magnitude of LST changes over the wind farms. In addition, atmospheric stability determines the sign and strength of the net downward heat transport as well as the magnitude of the background TKE. The study highlights the need for better understanding of atmospheric boundary layer and wind farm interactions, and for better parameterizations of sub-grid scale turbulent mixing in numerical weather prediction and climate models.

Keywords Wind farms · Atmospheric boundary layer · Land surface temperature · Turbulence kinetic energy

1 Introduction

Wind energy is widely acknowledged as a key to reducing the world's dependence on fossil fuels. It has experienced exponential growth in the recent years, especially in the United States (AWEA 2014). Wind farms are often sited over farmlands, such as in the Midwest and the Great Plains, where agricultural activity can be very sensitive to changes in microclimate effects due to wind turbine and atmospheric boundary layer (ABL) interactions (Armstrong et al. 2014). Therefore, understanding the dynamics and thermodynamics of such interactions and quantifying the effects of wind farms on surface/near-surface microclimate are of crucial importance for the sustainability and growth of renewable wind energy in the US and worldwide.

Due to lack of data from operational wind farms, modeling studies have been the main tool used to examine regional to global scale impacts of existing and hypothetical wind farms, despite large uncertainties in parameterizing sub-grid processes of turbine-ABL interactions (e.g., Baidya Roy et al. 2004; Keith et al. 2004; Adams and Keith 2007, 2013; Kirk-Davidoff and Keith 2008; Barrie

✉ Geng Xia
gxia@albany.edu

[1] Department of Atmospheric and Environmental Sciences, University at Albany, State University of New York, 1400 Washington Avenue, Albany, NY 12222, USA

[2] Atmospheric Sciences Research Center, State University of New York, Albany, NY, USA

[3] Centre for Atmospheric Sciences, Indian Institute of Technology Delhi, Hauz Khas, New Delhi 110016, India

[4] University of Illinois, 105 S. Gregory St, Urbana, IL 61801, USA

and Kirk-Davidoff 2010; Wang and Prinn 2010; Baidya Roy 2011; Cervarich et al. 2013). There have been several recent short-term observational studies at or near wind farms. Baidya Roy and Traiteur (2010) first used in situ observations from a wind farm in California to explore the relationship between ABL stability and changes in near-surface air temperature. They found that there is a net downward transport of warm air causing an increase in surface temperature in a stably stratified boundary layer environment. In the daytime when the lapse rate is negative, a net downward transport of cooler air causes a surface cooling effect. Rajewski et al. (2013) measured air temperature, surface fluxes and other variables in an Iowa wind farm as part of the Crop/Wind-Energy Experiment (CWEX) campaign. They found a small cooling (<0.75 °C) in 9 m air temperatures downwind of wind turbines during the day and a strong warming (up to 1.5 °C) at night. Smith et al. (2013) conducted a field campaign in a large wind farm in the Midwestern US and identified a strong surface warming of 1.9 °C in the wake of the wind farm at night but no substantial warming or cooling signals during the day.

As most field campaigns are relatively short and expensive, and their measurements are of limited spatial representativeness, satellite remote sensing provides a unique and cost-effective way to detect and quantify wind farm impacts with spatial details over large areas. Zhou et al. (2012) first used Moderate Resolution Imaging Spectroradiometer (MODIS) data from NASA's Terra and Aqua satellites to study wind farm impacts on land surface temperature (LST) over a region in west-central Texas, where four of the world's largest wind farms are located. They observed an areal mean warming effect of 0.31–0.70 °C over the wind farms at night but no noticeable effects during daytime. Cervarich et al. (2013) simulated LST changes for these four wind farms using the Weather Research and Forecasting (WRF) model under realistic boundary conditions. Although the simulated nighttime LST changes over the wind farms match MODIS observations in the spatial patterns, the magnitude of the warming effect is weaker.

Most studies indicate that wind farms cause a nighttime warming, with less consensus regarding daytime effects. Further details of seasonal and diurnal variations of such impacts, particularly their mechanisms in association with ABL characteristics (e.g., atmospheric stability, wind speed and turbulence kinetic energy), remain uncertain. Zhou et al. (2013a) found the wind farm-induced nighttime warming effect to be greater in summer than in winter and stronger at ~22:30 than at ~01:30 local time (LT). After analyzing reanalysis data, they proposed that the magnitude of the wind speed is likely the primary factor in determining the seasonal and diurnal variations of the warming effect.

This paper aims to further the work of Zhou et al. (2013a) by exploring likely physical mechanisms that determine the magnitude and variability of wind farm-induced temperature changes seasonally and diurnally over the same wind farms. For this purpose, observational wind profiles from a field campaign are used to examine the boundary layer turbulence characteristics in the wind farms. Our results show, in contrast with Zhou et al. (2013a), that the warming signal at ~01:30 is stronger than that at ~22:30 LT during the 1-year campaign period and the relative contribution of turbulence kinetic energy induced by the wind turbines (ETKE) to the background TKE plays a key role in determining the diurnal and seasonal wind farm impacts. This study helps to improve our understanding of ABL-turbine interactions and highlights the importance of realistically characterizing turbine-enhanced low-level atmospheric vertical mixing in modeling studies.

2 Data and methodology

2.1 Study region

We focus our study over a region (32.1°N–32.9°N, 101°W–99.8°W; Fig. 1) in west-central Texas that was previously studied by Zhou et al. (2013a). The database of Obstruction Evaluation/Airport Air-space Analysis (OE/AAA) from the Federal Aviation Administration (FAA) (https://oeaaa.faa.gov/oeaaa/external/portal.jsp) was used to identify each wind turbine and its geographic location. In total, there were 2358 wind turbines built in 2005–2008. The turbine locations were verified via Google Earth. The elevation of wind turbines and terrain topography mentioned in this paper are defined as the height above mean sea level.

2.2 Data

2.2.1 MODIS data

We use Collection 5 MODIS LST data as in Zhou et al. (2012, 2013a, b) from the NASA's Terra satellite launched in December 1999 and Aqua satellite launched in May 2002. MODIS provides four LST measurements every day over the study region, at ~22:30, ~01:30, ~10:30, and ~13:30 LT (Wan 2002). Although daily MODIS data are available, there are gaps and missing values. Hence, we choose 8-day LST products from Terra (MOD11A2) and Aqua (MYD11A2) that are averaged from 2 to 8 days of the daily products (Wan 2002) for the period 2003–2014. The MODIS LST data represent the best quality retrieval possible from clear-sky conditions over each 8-day period

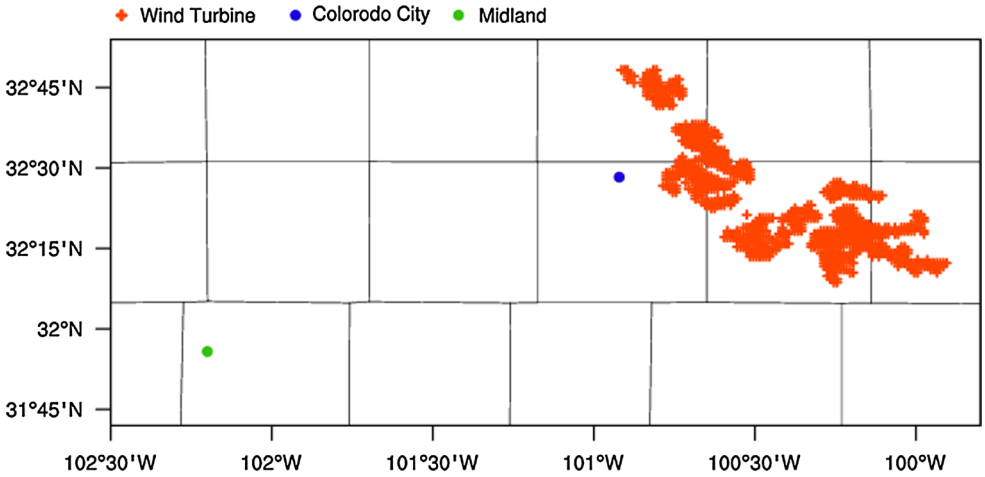

Fig. 1 Geographic locations (latitude and longitude) of individual wind turbines (*shaded* in *orange*) over the study region. Colorado City, TX (32.472°N, 100.92°W, the *blue dot*), where SoDAR measurements were taken in the WFIP field campaign, is located 11 km away from our targeted wind farms. The sounding station Midland, TX (WBAN: 23023, the *green dot*) lies ~135 km southwest of the wind farms

and have been proven to be of high quality in a variety of validation studies (Wan 2006). Compared to Zhou et al. (2012, 2013a), this study uses three additional MODIS measurements for the years 2012–2014. As Terra and Aqua have data starting in March 2000 and July 2002, respectively, a full year of data for both satellites are available for the period 2003–2014. We only consider this period to keep our diurnal comparisons consistent among the four MODIS measurements due to strong interannual LST variability.

2.2.2 *SoDAR wind profile and 3-D sonic flux measurements*

The US Department of Energy (DOE) and National Oceanographic and Atmospheric Administration (NOAA) sponsored a multi-year effort called the Wind Forecast Improvement Project (WFIP; Wilczak et al. 2014). WFIP's principle objective was to improve short-term (15 min–6-h) wind power production forecasts through the deployment of an enhanced observational network of surface and remote sensing instrumentation and the use of a state-of-the-art forecast modeling system. Instrument platforms and observation stations were deployed to ensure the complete capture of wind profiles from the surface through and beyond the top of the ABL (typically 1–3 km during daytime and 200–700 m during nighttime; Seidel et al. 2010). WFIP encompassed two regions and one of the regions, the Southern Study Area (SSA), covered most of Texas (Freedman et al. 2014). One WFIP station, Colorado City, TX (the blue dot in Fig. 1), is located 11 km away from the targeted wind farms.

The campaign site elevation is 673 m and was equipped with a suite of surface and remote sensing instrumentation including an Atmospheric Research Technology (ART) model VT-1 SoDAR and a R.M. Young model 81000 3-D sonic anemometer (more information regarding station instrumentation can be found in Freedman et al. 2014). The SoDAR has a vertical measurement range of 30–200 m at 10 m resolution. The data were processed on site and compiled into 10-min averages of wind speed and direction, as well as individual u, v and w components and respective standard deviations. The sonic anemometer, located at 3.25 m above ground level (AGL), used the eddy covariance system to measure the turbulence quantities u', v', w', and T' at a frequency of 10 Hz, enabling calculation of surface heat and momentum fluxes. The raw data were later compiled manually into 10-min averages. All data were been quality controlled in the field and through post-processing.

The field campaign lasted from July/2011 to September/2012 but only data from September/2011 to August/2012 were used to cover a full year. However, the SoDAR data were only available for 328 days and the sonic anemometer for 290 days due to instrument problems or severe weather events. For example, a lighting strike damaged all the equipment during the middle of June/2012 and it took a month to get everything back functioning again.

2.2.3 *Atmospheric sounding data*

High resolution radiosonde data from US upper air stations were obtained from the US NOAA/National Climatic Data Center (NCDC). The station closest to our study region is Midland (WBAN: 23023, the green dot in Fig. 1), which lies about 135 km southwest of the wind farms at an elevation of 873 m. Sounding data were reported every second at a vertical resolution of ~5 m with processed pressure, temperature and humidity, and generally launched twice daily (with the exception of extreme weather events when additional soundings were made) at 12:00 Greenwich Mean Time (GMT) and 00:00 GMT, which correspond to ~07:00 and ~19:00 LT in our study region.

Table 1 Seasonal variations in the percentage of SoDAR data availability with levels at the Colorado City, TX

Level (m)	SON		DJF		MAM		JJA		ANN	
	22:30	01:30	22:30	01:30	22:30	01:30	22:30	01:30	22:30	01:30
870	18.97	32.76	30.12	37.35	25.56	36.67	17.31	36.00	24.03	35.94
860	18.97	36.21	36.14	38.55	28.89	46.67	17.31	48.00	26.86	42.35
850	22.41	37.93	38.55	45.78	35.56	50.00	17.31	50.00	30.39	46.26
840	27.59	44.83	44.58	56.63	47.78	63.33	23.08	56.00	38.16	56.23
830	31.03	53.45	49.40	63.86	51.11	68.89	28.85	68.00	42.40	64.06
820	39.66	58.62	51.81	71.08	58.89	73.33	32.69	72.00	48.06	69.40
810	53.45	65.52	56.63	77.11	61.11	80.00	36.54	78.00	53.71	75.80
800	*58.62*	*68.97*	*62.65*	*79.52*	*66.67*	*87.78*	*46.15*	*86.00*	*60.07*	*81.14*
790	*63.79*	*79.31*	*68.67*	*86.75*	*77.78*	*87.78*	*55.77*	*88.00*	*68.20*	*85.77*
780	*68.97*	*82.76*	*80.72*	*89.16*	*82.22*	*91.11*	*63.46*	*90.00*	*75.62*	*88.61*
770	*75.86*	*87.93*	*85.54*	*91.57*	*88.89*	*95.56*	*86.54*	*94.00*	*84.81*	*92.53*
760	*82.76*	*91.38*	*89.16*	*96.39*	*94.44*	*98.89*	*90.38*	*98.00*	*89.75*	*96.44*
750	*86.21*	*93.10*	*96.39*	*98.80*	*95.56*	*98.89*	*94.23*	*100.0*	*93.64*	*97.86*
740	*96.55*	*98.28*	*100.0*	*100.0*	*98.89*	*100.0*	*98.08*	*100.0*	*98.59*	*99.64*
730	98.28	100.0	100.0	100.0	100.0	100.0	100.0	100.0	99.65	100.0
720	100.0	100.0	100.0	100.0	100.0	100.0	100.0	100.0	100.0	100.0
710	100.0	100.0	100.0	100.0	100.0	100.0	100.0	100.0	100.0	100.0
700	100.0	100.0	100.0	100.0	100.0	100.0	100.0	100.0	100.0	100.0

The measurements from 740 to 800 m (in italics) are the most active elevation range to study the ABL-turbine interactions. Only the data corresponding to nighttime MODIS measurements (~22:30, ~01:30) are shown

2.3 Data processing

2.3.1 MODIS LST data

Following Zhou et al. (2013a), we re-project the 8-day MODIS data archived by tile in Sinusoidal equal area projection into pixels at 0.01° resolution (~1.1 km by ~1.1 km). In total, there are 9600 pixels (120 columns × 80 lines) covering 2358 wind turbines in the study region. For every year, the data are combined into monthly means, which are then used to create monthly anomalies. Using three consecutive monthly anomalies, we obtain seasonal anomalies in DJF (Dec–Jan–Feb), MAM (Mar–Apr–May), JJA (Jun–Jul–Aug), SON (Sep–Oct–Nov), and the annual mean (ANN) anomalies for the period 2003–2014.

2.3.2 SoDAR data

The SoDAR measurements range from 30 to 200 m AGL, which correspond to elevations between 700 and 870 m. For comparison with MODIS data, the measurements taken at LT of ~10:30, ~13:30, ~22:30 and ~01:30 are chosen to create seasonal average profiles. Table 1 shows the seasonal variations in data availability at all vertical levels, which display a sharp increase in data gaps with increasing elevation (data availability <50 % above 800 m), a consequence of SoDAR signal degradation above 150 AGL measurement height.

Turbulence, the gustiness superimposed on the mean wind, can be visualized as irregular swirls of motion called eddies. An equation for calculating TKE is given as:

$$\mathrm{TKE} = \frac{1}{2}\left(\sigma_u^2 + \sigma_v^2 + \sigma_w^2\right) \quad (1)$$

where σ_u, σ_v, are σ_w are the 10-min averaged standard deviation of each wind component. We calculate TKE at four MODIS measurement times for each day and then composite them into seasonal and annual averages. In addition, we calculate TKE at every SoDAR time step to examine the diurnal cycle of TKE variations.

The average elevation of the wind turbines is 738.3 ± 27.5 m over the study region (Zhou et al. 2013b). Since both the hub-height and rotor diameter of a modern wind turbine are ~ 80 m, we take SoDAR measurements from 740 to 800 m (in red in Table 1) as the most active region to study ABL-turbine interactions. Consequently, results of wind speed and TKE profiles are shown within this elevation range.

2.3.3 Sonic data

Two variables derived from the sonic measurements were used to determine the near-surface stability condition during the campaign period. The first variable is the surface-layer stability parameter, given as:

$$\xi = z/L \tag{2}$$

where z is the measurement height and L is the Obukhov length (Obukhov 1946). The sign of ξ determines the near surface stability: positive (stable), negative (unstable) and zero (neutral). The absolute value of ξ indicates the strength of stability. The second variable is the friction velocity given as:

$$u^* = \left(\overline{u'w'}^2 + \overline{v'w'}^2\right)^{1/4} \tag{3}$$

where u', v' and w' are turbulence quantities for each velocity component (Stull 1988). Thus u^* can be treated as a surface turbulence scale. The less turbulent the surface layer, the smaller the magnitude of u^*. We average the 10-min daily data to obtain the seasonal diurnal cycle for both variables.

2.3.4 Sounding data

Radiosonde data are used to calculate virtual potential temperature profiles to determine atmospheric stability, which can affect the background TKE and energy transport. Since the focus of this study is the near-surface ABL, we only examine the lowest 1000 m of the atmosphere above the station. For unsaturated air with mixing ratio r, the virtual potential temperature is given by:

$$\theta_v = \theta \times \left(1 + 0.61^* r\right) \tag{4}$$

$$e = 6.11 \times 10^{\left(\frac{7.5\times T_d}{237.3+T_d}\right)} \tag{4a}$$

$$r = 0.622 \times \frac{e}{p - e} \tag{4b}$$

$$\theta = T \times \left(\frac{p_0}{p}\right)^{0.286} \tag{4c}$$

where T_d is dew point temperature, T is dry bulb temperature, e is vapor pressure, P is air pressure and P_0 is a reference pressure, which is set to 1000 hPa (Stull 1988).

2.4 Methodology

2.4.1 Estimate turbulence kinetic energy

The turbine-induced TKE, referred to as eTKE, is estimated based on three wind turbine parameterizations implemented in the Weather Research and Forecasting model (WRF). Figure 2 shows the TKE coefficients (C_{TKE}) of the three parameterizations. Even though mathematically similar, the three parameterizations differ in profile

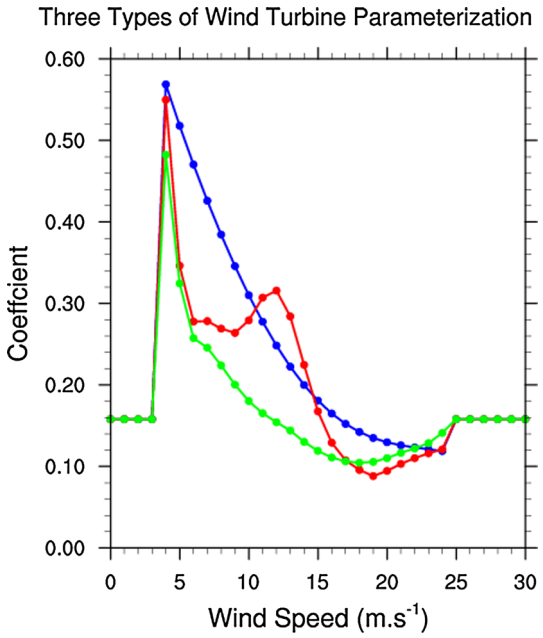

Fig. 2 TKE coefficient (C_{tke}) for three wind turbine parameterizations. The *green line* is the AK TKE coefficients, the *red line* is the CBR TKE coefficient and the *blue line* is the WRF TKE coefficient

shape because they represent different turbines from different manufacturers. The first parameterization is the default parameterization in WRF (Fitch et al. 2012). The second parameterization (AK) is developed by Adam and Keith (Adams and Keith 2013), while Cervarich et al. (2013) contribute to the third parameterization (CBR). The equation for eTKE is given below:

$$eTKE = \frac{1}{2} C_{TKE}(V) \rho A v^3 \tag{5}$$

$$C_{TKE}(V) = C_T(V) - C_p(V) \tag{5a}$$

where ρ is air density, A is the rotor swept area, v is wind speed, C_P is a wind speed-dependent power coefficient, and C_T is a wind speed-dependent thrust coefficient. The cut-in (4 ms^{-1}) and cut-out (25 ms^{-1}) speeds represent the range at which the wind turbine operates.

Divided right hand side by ρAv, Eq. (5) becomes

$$ETKE = \frac{1}{2} C_{TKE}(V) v^2. \tag{6}$$

This equation gives the ETKE (modified eTKE) generated by a wind turbine per unit mass of air per second. Similar to TKE, we calculate ETKE for each time step and composite the corresponding values into four MODIS measurement times and seasonal and diurnal profiles. The normalized ratio, (ETKE–TKE)/TKE, quantifies the relative importance of turbulent mixing caused by the wind turbine compared to that by the background atmosphere.

2.4.2 *Detect and attribute wind farm impacts using MODIS data*

Zhou et al. (2012) proposed two approaches to detect and quantify wind farm impacts on LST between two periods (before and after the wind farms are built). As the wind turbines in our study region were built between 2005 and 2009, the two periods are defined as the pre-turbine period (2003–2004) and the post-turbine period (2010–2014). The first method is to examine the spatial coupling of pixel-level LST changes between these two periods with the geographic layout of wind turbines. The second is to compare the areal mean LST differences between wind farm pixels (WFPs) versus nearby non-wind farm pixels (NNWFPs) during these two periods. WFPs are defined as the pixels containing at least one wind turbine and NNWFPs are those that are between 6 and 9 pixels away from WFPs (Zhou et al. 2012, 2013a). Turbulence generated by the wind turbine decreases farther downwind from the rotor blades. Baidya Roy et al. (2004), Petersen et al. (1997) and Barthelmie (2010) state that a distance of ten rotor diameters (about 1 km for typical wind turbines with ~80 m rotor diameter) downstream is enough for the flow to recover from the turbine wake-induced turbulence. Therefore, the defined NNWFPs are far enough from WFPs to eliminate downstream impacts.

Here we use the same approaches as Zhou et al. (2012, 2013a) but focus primarily on the 1-year period during which the WFIP data are available. However, MODIS LST show strong interannual variability (high-frequency) controlled primarily by year-to-year regional to large-scale meteorological conditions, while the wind farm effect on LST is a small and persistent (low-frequency) signal. For this reason, Zhou et al. (2012, 2013a, b) used (a) multi-year averages or an empirical orthogonal function (EOF) analysis at pixel level, and (b) an estimated linear trend from year-to-year time series at regional aggregated level, to minimize the high-frequency LST variability. As the emphasis of this study is on the WFIP field campaign period, we apply an EOF analysis to the seasonal and annual LST anomalies to minimize some of the extreme high-frequency and localized LST signals for the same purposes. Through this high-frequency filtering, we reconstruct the LST data from the first several EOF components, which explain >95 % of the total variance of the original MODIS LST anomalies.

For the first method, the LST anomalies for the pre-turbine period (2003–2004) are subtracted from the LST anomalies for the post-turbine period (2010–2014). Figure 3 shows the average JJA LST anomaly for the 5-year post-turbine period relative to that for the 2-year pre-turbine period for both daytime and nighttime, whereas Fig. 4 demonstrates the JJA LST anomalies at nighttime for each individual year from 2010 to 2014. The individual years including the WFIP field campaign period are used to demonstrate the effectiveness of our approaches. If the development of wind farms has impacts on LST, the observed LST change should couple spatially with the wind turbines as shown in Zhou et al. (2012, 2013a).

For the second method, we use the areal mean LST differences (WFPs minus NNWFPs), denoted as ΔLST, between the post- and pre-turbine periods to quantify the wind farm impact on LST. We assume that WFPs and NNWFPs are close enough to share similar atmospheric and land surface boundary conditions, and so their LST difference represents the wind farm impacts. For the field campaign period, the post-turbine ΔLST is only calculated from the LST in the particular year. Subtracting the pre-turbine ΔLST from the post-turbine ΔLST removes the LST differences due to differences in land surface properties over these two groups of pixels. If the wind farms modify local temperature, the ΔLST change should be consistent with those estimated using the first method.

3 Results and discussion

3.1 Changes in LST

Zhou et al. (2013a) have extensively analyzed the diurnal and seasonal variations in wind farm-induced LST changes for the period of 2003–2011. Their results show that (a) there is a spatial coupling between the nighttime warming and the layout of the wind turbines, with the best spatial coupling in JJA, and (b) the nighttime warming effect is stronger at ~22:30 than ~01:30 LT. Here we first briefly discuss some key results with the use of additional years of MODIS data and then discuss the differences from previous findings.

Figure 3 shows the spatial patterns of pixel-level LST changes in JJA at ~22:30, ~01:30, ~10:30, and ~13:30 LT between the post-turbine (2010–2014) and pre-turbine (2003–2004) period. There is a strong spatial coupling between the warming signal and the wind turbines, with a maximum warming up to 1.35 °C at nighttime. The daytime LST anomalies, however, exhibit no spatial coupling with the wind turbines, suggesting that the wind farms have negligible impacts at daytime or it is difficult to detect the daytime wind farm signal (see additional discussion later in this section). Among the four seasons, the nighttime spatial coupling is strongest in JJA (figures for other seasons are not shown to avoid redundancy), consistent with Zhou et al. (2013a). Table 2a quantifies the wind farm impacts in terms of the seasonal ΔLST values (WFPs minus NWFPs) between

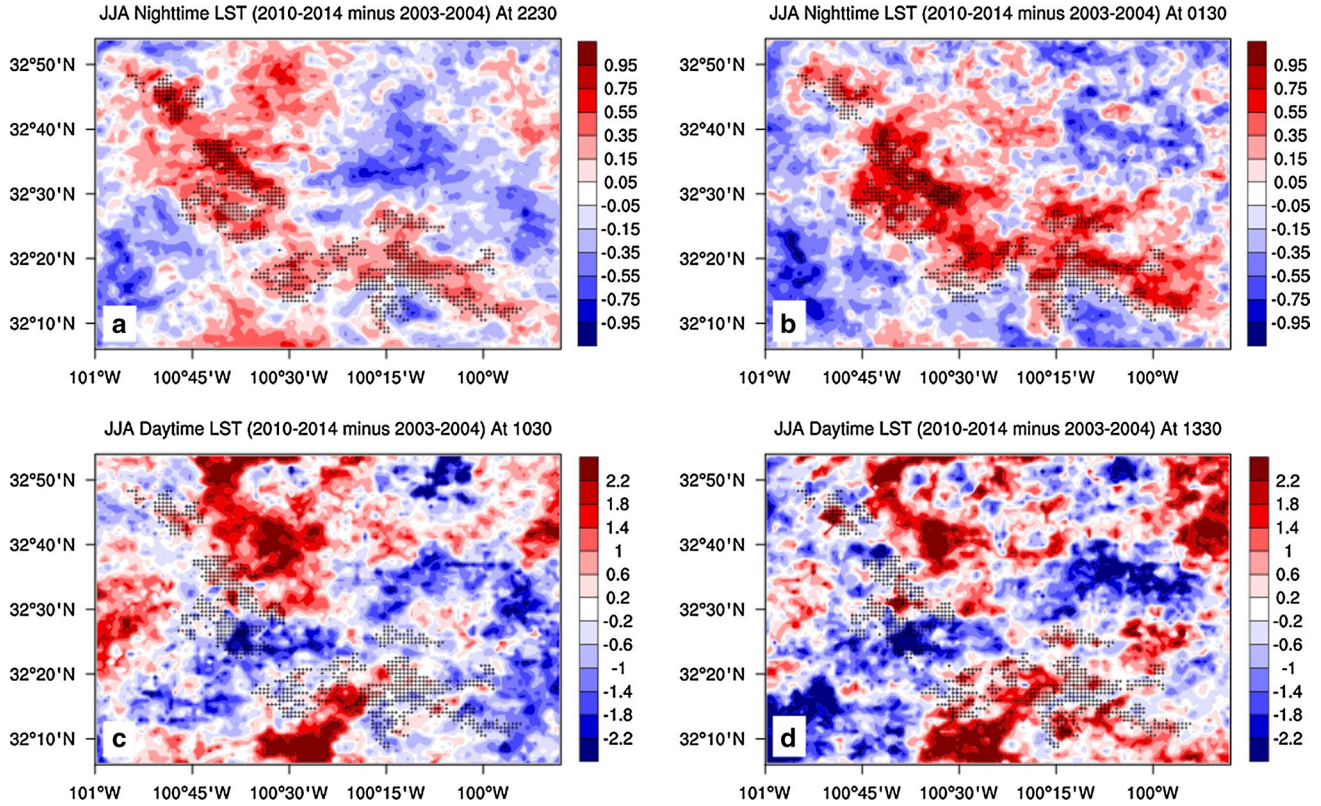

Fig. 3 MODIS JJA LST anomaly differences (°C) (2010–2014 averages minus 2003–2004 averages) at **a** ~22:30 LT (nighttime), **b** ~01:30 LT (nighttime) and **c** ~10:30 LT (daytime) and **d** ~13:30 LT (daytime). *Pixels with plus symbol* have one or more wind turbines at 0.01° resolutions

the post- and pre-turbine periods for both Terra and Aqua measurements. A positive ΔLST, which indicates a warming effect over the wind farms relative to their immediate surrounding non-wind farms, is consistently seen across all seasons at both ~22:30 and ~01:30 LT. In contrast, a negative ΔLST is observed for five of eight cases (two MODIS daytime measurements per season multiplied by four seasons), suggesting a possible cooling effect over the wind farms.

Overall the strong spatial coupling of the warming signal with the turbines at nighttime and the absence of this coupling at daytime are consistent with previous studies (Zhou et al. 2012, 2013a). However, although the magnitude of nighttime warming effect is strong at both ~22:30 and ~01:30 LT, there is no consistency in terms of temporal evolution from ~22:30 to ~01:30 LT across all seasons. Therefore, it is difficult to conclude that the warming effect is larger at ~22:30 than ~01:30.

Next, we focus on the individual year to examine the wind farm impacts on LST. Since the daytime impact cannot be confidently quantified and attributed, we will focus exclusively on the nighttime impact. Figure 4 shows the pixel-level JJA LST differences between the 2003 and 2004 averages and each individual year of 2010–2014 at ~22:30 and ~01:30 LT. There is a strong spatial coupling between the wind turbines and the LST changes for five consecutive years at both ~22:30 LT and ~01:30 LT, which is consistent with the multi-year average LST changes (Fig. 3) and previous results (Zhou et al. 2013a). However, the spatial coupling is generally stronger at 01:30 LT than at ~22:30 LT, especially after 2011. In particular, the year 2012 illustrates different features from the other years as well as from the multi-year average. For example, the magnitude of the wind farm warming effect in 2012 at both nighttime measurements (~22:30 and ~01:30 LT) are smaller than that in the other 4 years, possibly due to changes in atmospheric patterns. Further investigation of this difference, however, is beyond the scope of this study as our focus here is to discern the physical connections between the observed LST changes and atmospheric wind profiles during the WFIP field campaign year.

Table 2b lists the seasonal ΔLST values between the field campaign year and the pre-turbine period. The nighttime warming signal is seen at both ~22:30 and ~01:30 LT in all seasons, with the following features: (a) the strongest warming is in SON; (b) the warming increases from ~22:30 LT to ~01:30 LT in DJF, MAM and JJA but decreases in

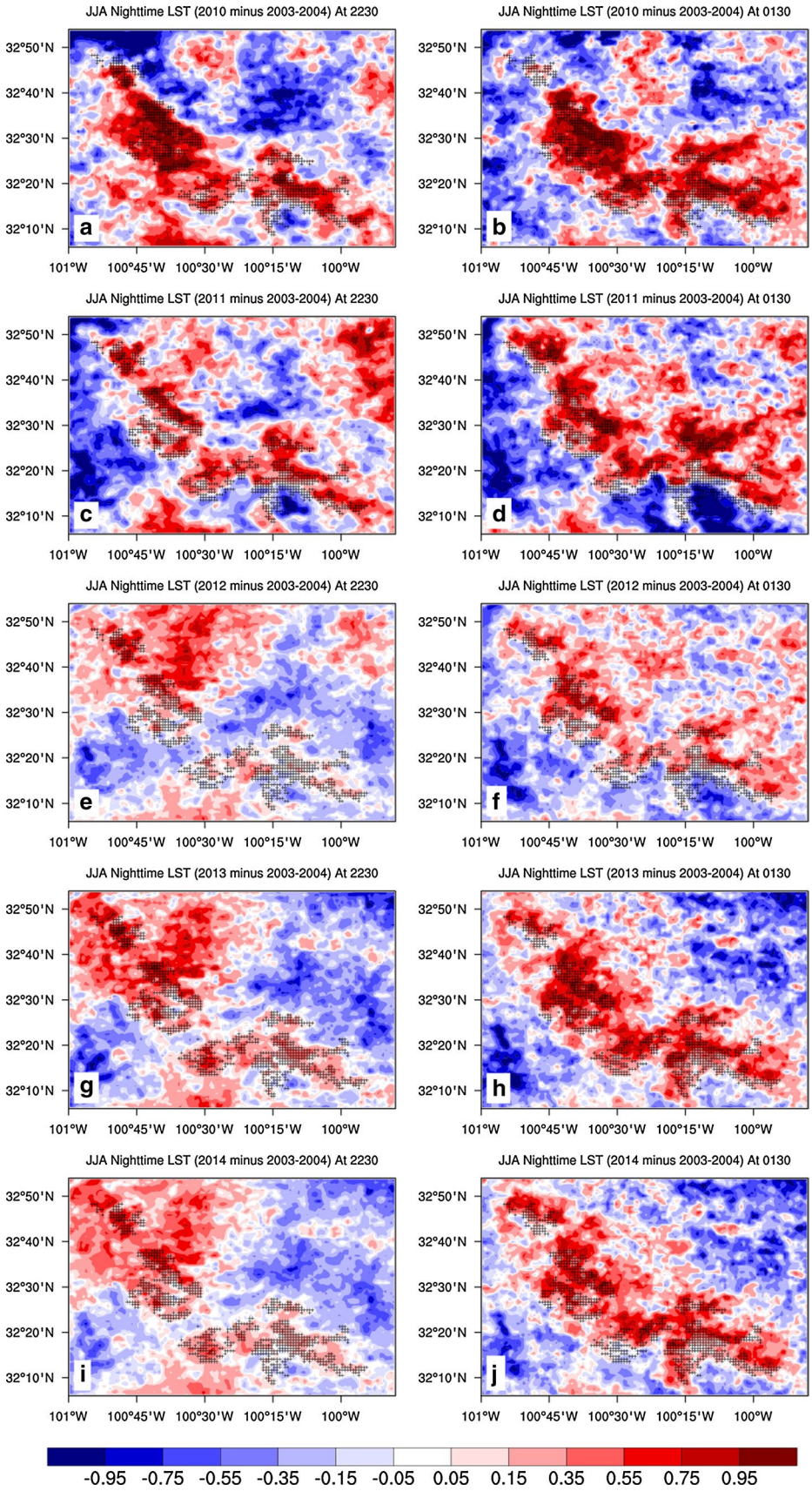

Fig. 4 MODIS JJA LST anomaly differences (°C) (individual years of 2010–2014 minus 2003–2004 averages) at **a**, **c**, **e**, **g**, **i** ~22:30 LT (*left panels*) and **b**, **d**, **f**, **h**, **j** ~01:30 LT (*right panels*). *Pixels with plus symbol* have one or more wind turbines at 0.01° resolutions

Table 2 Areal mean LST differences (°C) between WFPs and NNWFPs (WFPs minus NNWFPs)

Season	Nighttime		Daytime	
	~22:30	~01:30	~10:30	~13:30
(a) 2010–2014 averages minus 2003–2004 averages				
SON	0.37	0.17	0.05	−0.08
DJF	0.28	0.23	0.28	0.07
MAM	0.26	0.53	−0.39	−0.11
JJA	0.38	0.45	−0.38	−0.13
ANN	0.32	0.34	−0.11	−0.06
(b) Field campaign year minus 2003–2004 averages				
2011, SON	0.39	0.28	0.11	−0.21
2012, DJF	0.14	0.16	0.03	0.07
2012, MAM	0.10	0.28	−0.46	−0.23
2012, JJA	0.19	0.28	−1.19	−0.73
ANN	0.20	0.25	−0.38	−0.27

SON; (c) the annual average warming rate is stronger at ~01:30 LT than at ~22:30 LT. In contrast, the daytime LST exhibits a substantial cooling effect in five of the eight cases, particularly in JJA/2012 and MAM/2012. As discussed previously, there is no spatial coupling between the LST changes and the wind turbines and the areal mean ΔLST values also vary strongly from year to year, making it difficult to attribute this cooling primarily to the wind turbines. It is likely that our spatial coupling method may not work well during the daytime when high-frequency LST variations maximize (see more discussion later).

3.2 Relationship between LST changes and wind speed

Figure 5 illustrates the diurnal wind speed variations during the field campaign year. A nocturnal low-level jet (LLJ) is evident in the seasonal composites. In general, the LLJ starts to develop after sunset, maximizes around 22:00 LT, and dissipates in the early morning. Also the height–time cross sections of LLJ vary seasonally. Compared to other seasons, the nocturnal LLJ is stronger and penetrates lower in MAM/2012.

Figure 6 shows the seasonal variations in wind speed profiles at the two MODIS nighttime measurement times. The wind speed is consistently higher at ~22:30 LT than at ~01:30 LT for all levels. The black horizontal dashed lines show a typical rotor plane covering the most active layer of turbine-generated turbulence, given an 80 m hub height. Within this range, the wind speed varies from 6.8 to 11.5 ms^{-1}, which correspond to the maximum efficiency of the wind turbines (Fig. 2). The wind speed across the rotor plane ranges between 7.0 and 10.5 ms^{-1} in SON/2011, 6.8–9.8 ms^{-1} in DJF/2012, 7.6–11.5 ms^{-1} in MAM/2012, and 7.4–10.5 ms^{-1} in JJA/2012. Overall, the seasonal differences in wind speed between ~22:30 and ~01:30 LT around the hub-height region are small.

Figure 7 illustrates the seasonal variations of radiosonde-measured wind speed at 19:00 and 07:00 LT. The nocturnal LLJ is located 200–600 m (elevation 1073–1473 m) AGL with a maximum wind speed of ~12 ms^{-1}. Interestingly, the seasonal wind profiles over the lowest 200 m (elevation 1073 m) vary substantially at 19:00 LT, but are mostly similar at 07:00 LT. For example, the morning hub-height wind speed is 6.45 ms^{-1} in SON/2011, 6.84 ms^{-1} in DJF/2012, 6.96 ms^{-1} in MAM/2012, and 6.31 ms^{-1} in JJA/2012. This small seasonal difference agrees well with the SoDAR measurements.

Using hourly 50 m reanalysis wind data, Zhou et al. (2012, 2013a) showed that the wind speed is stronger in JJA than in DJF and at ~22:30 than ~01:30 LT, and the MODIS data depicted a stronger warming effect over the wind farms in JJA and at ~22:30 LT as well. Hence, they proposed that the seasonal and diurnal variations in the magnitude of wind speed primarily determine those in the wind farm-induced warming effect. If this were true, we would not see a stronger warming effect at ~01:30 than ~22:30 LT (Table 2) during most seasons as the SoDAR wind speed is always stronger at the latter than the former (Fig. 6). Furthermore, both the field campaign data and the radiosonde observations show that the seasonal wind speed differences between ~22:30 and ~01:30 LT around the hub-height region are small, which cannot explain the large seasonal and diurnal variations in the nighttime warming effect observed over the wind farms. Our results in next section suggest that the relative contribution of ETKE versus TKE may play a more important role.

3.3 Relationship between LST changes and (ETKE–TKE)/TKE

Tables 3 and 4 list the seasonal variations in TKE and ETKE at the four MODIS measurement times. TKE represents the background state of turbulence (background TKE) inferred from the SoDAR, whereas ETKE represents the turbine-induced turbulence. As our analysis consists of three wind turbine parameterizations, it is not practical to show all the results but their ensemble means. At nighttime, the annual averaged TKE ranges from 0.40 to 0.64 m^2s^{-2} and the corresponding ETKE varies from 8.71 to 14.38 m^2s^{-2}. On average, the values of ETKE are about twenty times those of TKE, and both ETKE and TKE decrease from ~22:30 to ~01:30 LT in all seasons. At daytime, the annual mean TKE is between 0.83 and 1.47 m^2s^{-2} and the corresponding ETKE is between 7.75

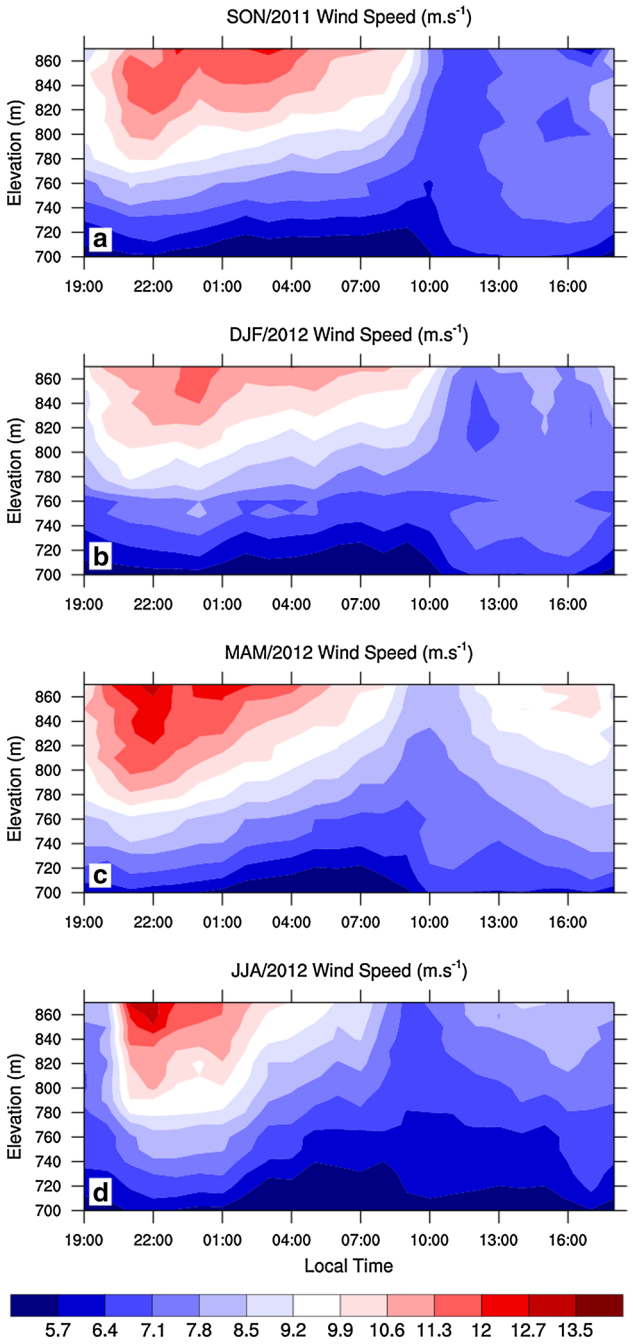

Fig. 5 Seasonal variations in the diurnal cycle of wind speeds measured at Colorado City, TX for the period Sep/2011–Aug/2012: **a** SON/2011, **b** DJF/2012, **c** MAM/2012, and **d** JJA/2012

and 8.75m^2s^{-2}. On average, the values of ETKE are about 6–9 times those of TKE, and both ETKE and TKE increase from ~10:30 to ~13:30 LT in all seasons. In terms of the diurnal range, especially from ~01:30 LT to ~13:30 LT, the annual TKE increases from a minimum of 0.40 m^2s^{-2} to a maximum of 1.47 m^2s^{-2}, whereas the annual ETKE decreases from 13.63 to 7.83 m^2s^{-2}.

Figures 8 and 9 describe the seasonal variations in the diurnal cycle of TKE and ETKE. The entire layer depth is plotted to illustrate the potential effect from taller turbines, while the green dashed lines (740–800 m) indicate the most active layer of turbine-generated turbulence. The background TKE is stronger during the daytime than during the nighttime, which is similar to that measured by Rhodes and Lundquist (2013) using ground-based Doppler Lidar. The daytime solar heating at the surface greatly increases the background daytime TKE and consequently causes the night-to-day TKE enhancement. Such features are most evident by comparing the TKE from winter to summer when the solar heating changes from the weakest to the strongest. The nighttime TKE value around the hub-height region is largest in MAM/2012 and smallest in SON/2011. As expected, the diurnal and vertical structures of ETKE resemble mostly those of wind speed (Fig. 5), which largely determines the magnitude of turbine-enhanced turbulence. Unlike TKE, ETKE decreases from nighttime to daytime due to the decay of the nighttime LLJ. At nighttime, there is generally a decreasing trend in TKE and ETKE from 22:00 to 07:00 LT at all levels.

The normalized ratio, (ETKE–TKE)/TKE, quantifies the relative contribution of the turbine-induced turbulence versus the background TKE. The larger the ratio, the more contribution of the former relative to the latter. Overall the ratios at the four MODIS measurement times are much smaller during the daytime (~10:30 and ~13:30 LT) than during the nighttime (~22:30 and ~01:30 LT), regardless of seasons (Tables 3, 4). The annual mean ratio is 20.30 at nighttime while it drops to 6.43 at daytime, suggesting that the wind farm impact, if any, is much larger and thus more detectable at nighttime than at daytime. This agrees with the asymmetric day–night differences in the MODIS LST changes observed over the wind farms (Table 2; Fig. 3).

Figure 10 shows the diurnal cycle of the (ETKE–TKE)/TKE ratio for all the seasons during the campaign period. Again the ratio shows a significant day–night contrast as in Tables 3 and 4. At nighttime, the seasonal variations of ratio strongly correlate with those in the LST warming signal. For example, SON/2011 has both the strongest warming signal (0.33 °C, averaged over ~22:30 and ~01:30 LT) and the largest ratio (46.3, averaged over ~22:30 and ~01:30 LT). The temporal variations in (ETKE–TKE)/TKE also correlate with those in the LST signal at nighttime—both the warming rate and the ratio of (ETKE–TKE)/TKE increase from ~22:30 to ~01:30 LT. For instance, the annual mean ΔLST rises from 0.20 °C at ~22:30 to 0.25 °C at ~01:30 LT and the corresponding ratio increases from 19.4 to 21.3. Note that the relative large nighttime ratio in SON is due to the smallest TKE compared to other seasons (Fig. 8). Particularly, the ratios for all seasons indicate a vigorous signal of intensification and penetration from the

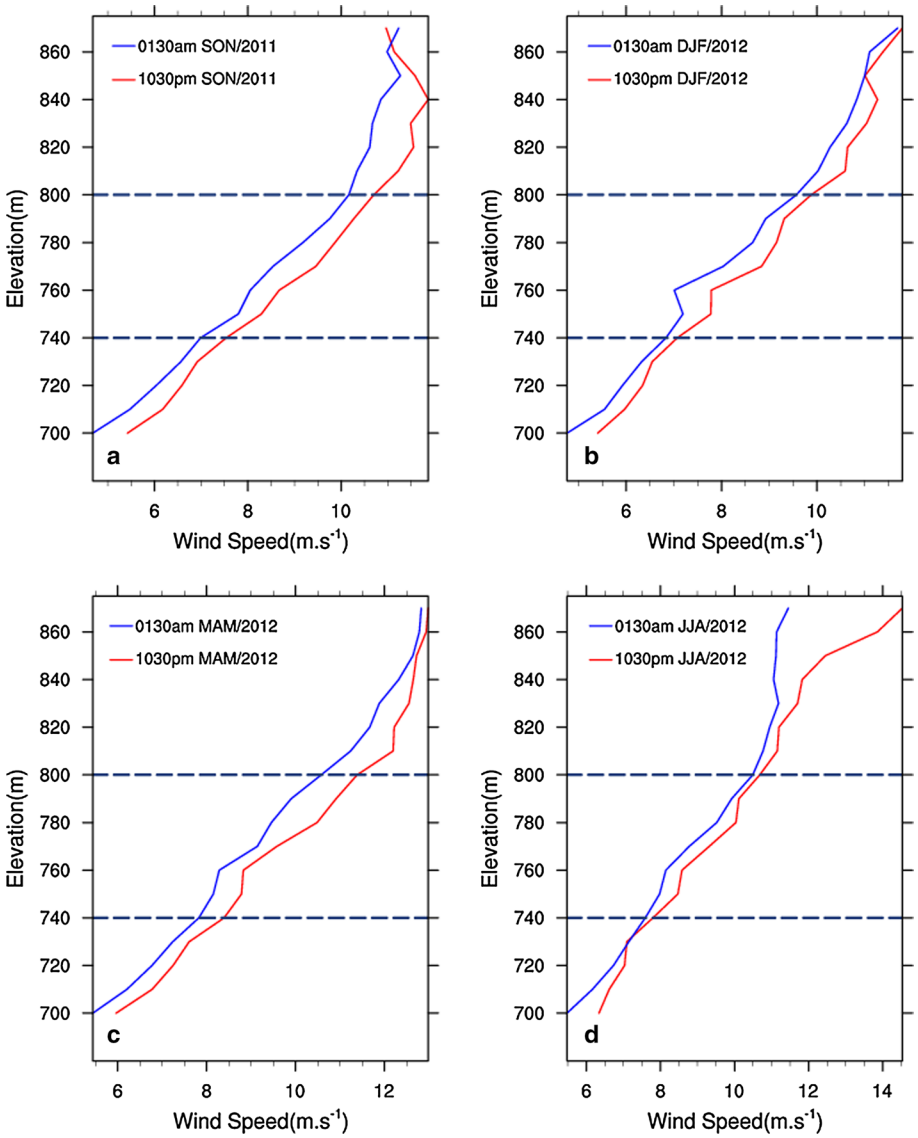

Fig. 6 Seasonal variations in wind speed profiles measured at Colorado City, TX at MODIS nighttime measurement times (~22:30 and ~01:30 LT) for the period Sep/2011–Aug/2012: **a** SON/2011, **b** DJF/2012, **c** MAM/2012, and **d** JJA/2012. The *dashed lines* (740–800 m) indicate the most active layer of turbine-generated turbulence

upper layer to the ground between 22:00 and 01:00 LT, meaning that more energy is being transported down to the surface during that time period, which mostly agrees with the LST changes shown in Table 2b.

Overall, our results indicate that the relative importance of ETKE to TKE plays an essential role in determining the wind farm impacts, not only in the magnitude of day–night LST change but also in the seasonal and temporal variations in the nighttime warming effect. However, there are two exceptions. Among the two MODIS nighttime measurement times (~22:30 and ~01:30 LT), the nighttime warming effect is stronger at ~22:30 LT in SON/2011 while the (ETKE–TKE)/TKE ratio is stronger at ~01:30 LT. Among the four seasons, DJF/2012 has the ratio larger than MAM/2012 and JJA/2012 but its warming effect is smallest. These exceptions are likely due to data uncertainties and limitations of our approaches (more discussion in Sect. 3.5). In addition, we use the (ETKE–TKE)/TKE ratios at the four specific MODIS measurement times to explain the temporal or seasonal variations of wind farm-induced impacts on LST. However, LST changes gradually rather than instantaneously in response to a forcing. For instance, the LST difference between ~22:30 and ~01:30 LT reflects the change in thermal and energy budget due to the turbine-enhanced vertical mixing during this 3-h period instead of at the two specific time steps. That is why we also plot the results at every SoDAR time step to illustrate their whole diurnal cycle. It is also reasonable to assume that other factors (e.g., atmospheric stability) will also play a key role when the ratio differences between these two times are too small or within the range of data uncertainty. More and longer

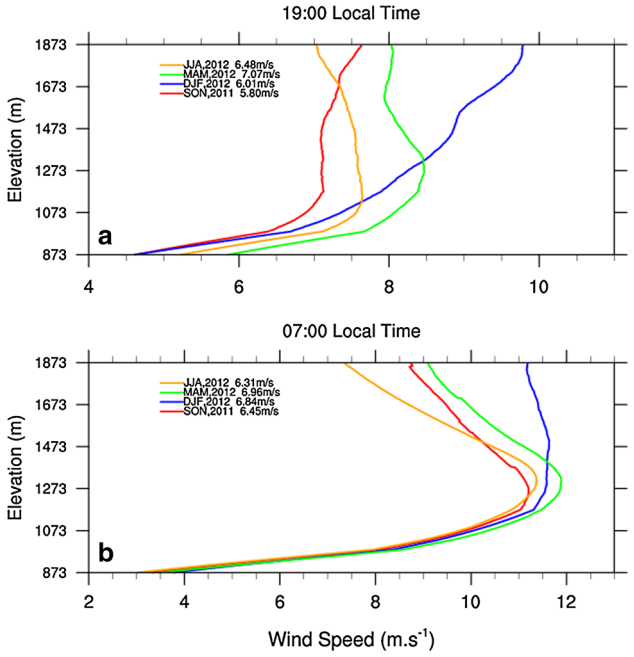

Fig. 7 Seasonal variations of wind profiles over the first 1000 m atmospheric boundary layer measured at Midland, TX (WBAN: 23023; Station height: 873) at **a** 19:00 and **b** 07:00 LT for the period Sep/2011–Aug/2012. The 80 m hub-height wind speeds are labeled in the figure

observations are needed to fully understand the complex processes involved.

3.4 Relationship between LST changes and atmospheric stability

Zhou et al. (2012, 2013a) only examined MODIS data to quantify wind farm impacts. Baidya Roy and Traiteur (2010) analyzed sounding data near their wind farms and found that there is a positive lapse rate at 04:00 LT and a negative lapse rate at 16:00 LT over the wind turbine wake layer, and the corresponding near-surface air temperature shows a warming signal at 04:00 LT and a cooling effect at 16:00 LT. The diurnal difference points to a positive correlation between the wind farm impact and atmospheric stability. However, their period of record is only 1.5 months, which is too short to draw a definitive conclusion applicable to other wind farms.

Figure 11 shows the virtual potential temperature profile from Midland, TX (the nearest upper air station) at 07:00 and 19:00 LT. Under undisturbed conditions, the atmosphere is generally either neutral or unstable at 19:00 LT but under quiescent conditions becomes stable at 07:00 LT due to nighttime radiative cooling. In addition, SON/2011 has the largest vertical gradient of virtual potential temperature, about 23.09 K/km over the first 1000 m layer at 07:00 LT. This indicates that SON/2011 has the most stable surface layer at nighttime, which in return will produce the most effective thermal mixing by the wind turbines and consequently cause the strongest warming signal in SON/2011 (Baidya Roy and Traiteur 2010; Baidya Roy 2011; Harris et al. 2014; Slawsky et al. 2015). The temperature gradient of MAM and JJA are smaller than SON but comparable to each other with gradients of 14.72 and 13.45 K/km, respectively, and correspondingly the LST changes are also similar for these two seasons. DJF/2012 has the second largest gradient, about 20.47 K/km, but shows the smallest warming signal as discussed previously. Note that the virtual temperature gradients are estimated from the lowest 200 m layer (873–1073 m). Given the limit of two sounding measurements per day and the large distance from the campaign site, we cannot confidently estimate the seasonal atmospheric stability at Colorado City from the sounding data alone. However, if the surface stability derived from the sonic anemometer agrees with the radiosonde data, we will be more certain about the stability condition during the campaign period.

Figure 12 shows seasonal variations of surface-layer stability parameter (ξ) and friction velocity (u^*) in the diurnal cycle measured at the Colorado City during the campaign period. The larger the ξ and the smaller the u^*, the more stable the near surface atmosphere. Generally, ξ tends to be positive (stable) during the nighttime and becomes negative (unstable) during the daytime. The average ξ values during the nighttime (19:00–07:00 LT) indicates that SON/2011 has the largest positive ξ (0.33), followed by DJF/2012 with MAM/2012 and JJA/2012 being comparable to each other. As for u^*, not surprisingly, higher values occur during the day than during the night, meaning the near-surface atmosphere is more turbulent (convective) at daytime than at nighttime. Similarly, the smallest average u^* (0.20 ms^{-1}) during the nighttime (19:00–07:00 LT) indicate that SON/2011 has the most stable surface layer compared to the other three seasons. Thus, the seasonal near surface stability inferred from the sonic data agrees well with that from the radiosonde data. In addition, the near surface tends to become more stable as u^* decreases (ξ increases) between ~22:30 and ~01:30 LT, which is consistent with the increasing warming effect shown in Table 2b.

Both Fig. 8 and Table 3 demonstrate that the nighttime background TKE is largest but comparable in MAM/2012 and JJA/2012, followed by DJF/2012, and least in SON/2011. This relationship is supported by the seasonal changes in the near-surface stability (Fig. 12) as well as in the virtual potential profile (Fig. 11). Thus we can reasonably predict that during the campaign period, SON/2011 has the most stable nocturnal near-surface ABL (the lowest 1000 m), followed by DJF/2012, MAM/2012 and

Table 3 Seasonal and diurnal variations in nighttime TKE, ETKE and (ETKE–TKE)/TKE with levels at Colorado City, TX

Time	SON, 2011		DJF, 2012		MAM, 2012		JJA, 2012		ANN	
	22:30	01:30	22:30	01:30	22:30	01:30	22:30	01:30	22:30	01:30
TKE by level (m)										
800	0.28	0.23	0.62	0.58	0.89	0.81	0.81	0.65	0.64	0.58
790	0.24	0.24	0.59	0.53	0.88	0.72	0.79	0.62	0.62	0.53
780	0.29	0.23	0.57	0.52	0.87	0.71	0.81	0.58	0.63	0.51
770	0.34	0.23	0.56	0.50	0.82	0.69	0.78	0.55	0.62	0.50
760	0.28	0.19	0.56	0.49	0.73	0.66	0.75	0.58	0.57	0.48
750	0.26	0.19	0.55	0.49	0.73	0.58	0.76	0.57	0.56	0.45
740	0.26	0.16	0.49	0.45	0.70	0.51	0.62	0.52	0.51	0.40
ETKE by level (m)										
800	14.63	13.72	12.98	12.64	15.69	14.24	14.53	13.09	14.38	13.63
790	14.02	12.96	12.07	11.67	15.01	13.14	14.05	12.95	13.74	12.63
780	13.33	11.97	11.89	11.21	14.12	12.50	14.39	12.36	13.31	11.94
770	12.71	10.55	11.41	10.41	12.88	11.82	12.58	11.19	12.37	10.99
760	11.24	9.82	9.67	8.65	11.66	10.47	11.36	10.16	10.94	9.73
750	10.28	9.35	9.77	8.90	11.39	10.13	11.19	9.73	10.61	9.51
740	8.96	7.97	8.77	8.33	10.68	9.56	10.13	9.14	9.59	8.71
Ratio by level (m)										
800	52.11	58.99	20.0	20.81	16.68	16.68	17.04	20.84	21.45	22.50
790	58.38	52.28	19.41	21.18	16.11	17.23	16.76	19.98	21.33	22.81
780	45.29	51.90	19.86	20.25	15.28	16.50	16.85	20.44	20.26	22.32
770	36.89	44.25	19.25	19.73	14.70	16.14	15.14	19.41	18.96	21.20
760	29.48	51.47	16.30	16.72	14.88	14.79	14.16	16.58	18.09	19.35
750	38.08	47.46	16.75	17.28	14.55	16.41	13.76	16.09	17.80	19.97
740	34.10	47.47	16.79	17.62	14.28	17.64	15.43	16.55	17.75	20.70

Results are the ensemble means of TKE, ETKE and (ETKE–TKE)/TKE averaged from three wind turbine parameterizations. Only the data corresponding to nighttime MODIS measurements (~22:30, ~01:30) are shown

JJA/2012. These seasonal characteristics show a clear positive correlation between atmospheric stability and TKE, indicating a less turbulent atmosphere within a more stable ABL.

We hypothesize that it is the downward transport of heat induced by the turbulence mixing from the operational wind farms that causes the LST changes. During the daytime, the mixing transports cooler air downward as well as warmer air upward. Since the background TKE is very strong during the day, the negative downward heat transport due to the turbines will be diluted in the surrounding environment, and thus any wind farm impact would be weak. At nighttime, however, warmer air is transported downward while cooler air is lifted up. Since the atmosphere is relatively stable, the positive heat transport from the wind turbines can easily penetrate to the surface, producing a warming LST anomaly.

The virtual potential temperature gradient and the surface-layer stability parameter determine the sign and strength of the net downward heat transport for a given vertical mixing, and TKE and ETKE determine the magnitude of the net heat transport. Therefore, the large contrast between TKE and ETKE makes it easier to detect the wind farm impacts at nighttime, while the small ratio makes it hard to differentiate the small turbine-induced LST signal from the large background LST (i.e., the LST variations without the presence of wind farms) variations at daytime. This is consistent with other field campaign studies (e.g., Rajewski et al. 2013; Smith et al. 2013) that have also reported a strong and consistent warming effect in the wind farm wakes at nighttime but small or negligible wind farm effects during the day.

3.5 Uncertainties in data and methodology

Zhou et al. (2013a) analyzed MODIS LST data uncertainties and errors and found consistent results under various quality controls. They also excluded potential impacts of surface topography and land use change on the observed LST changes over the wind farms. Next we will focus on some new perspectives that are not addressed in the previous studies.

Table 4 Seasonal and diurnal variations in daytime TKE, ETKE and (ETKE–TKE)/TKE with levels at Colorado City, TX

Time	SON, 2011		DJF, 2012		MAM, 2012		JJA, 2012		ANN	
	10:30	13:30	10:30	13:30	10:30	13:30	10:30	13:30	10:30	13:30
TKE by level (m)										
800	0.63	1.32	0.73	1.27	1.30	1.67	1.37	1.76	0.97	1.47
790	0.62	1.27	0.70	1.24	1.25	1.66	1.34	1.74	0.94	1.45
780	0.60	1.28	0.70	1.23	1.20	1.63	1.30	1.73	0.91	1.44
770	0.58	1.20	0.69	1.18	1.19	1.62	1.29	1.69	0.90	1.39
760	0.58	1.15	0.67	1.20	1.13	1.55	1.26	1.66	0.87	1.36
750	0.56	1.09	0.65	1.21	1.13	1.53	1.22	1.60	0.85	1.33
740	0.54	1.02	0.63	1.20	1.12	1.50	1.16	1.59	0.83	1.30
ETKE by level (m)										
800	7.13	7.63	9.49	8.69	8.84	10.63	7.73	7.89	8.38	8.75
790	7.00	7.54	8.97	8.76	8.67	10.31	7.47	7.91	8.12	8.68
780	7.15	7.38	8.79	8.69	8.79	9.87	7.44	7.66	8.12	8.48
770	7.13	7.59	8.70	8.54	8.73	9.40	6.98	7.12	8.01	8.27
760	7.07	7.49	7.74	8.08	8.64	9.00	6.91	6.72	7.67	7.95
750	7.23	7.66	8.25	8.53	8.81	8.88	6.97	6.75	7.92	8.09
740	6.86	7.24	8.17	8.42	8.69	8.52	6.83	6.64	7.75	7.83
Ratio by level (m)										
800	10.37	4.29	12.07	5.86	5.80	5.36	4.65	3.49	7.66	4.95
790	10.27	4.92	11.75	6.04	5.95	5.20	4.58	3.54	7.63	4.99
780	10.92	4.78	11.59	6.08	6.30	5.05	4.71	3.43	7.90	4.90
770	11.22	5.33	11.62	6.23	6.36	4.81	4.48	3.04	7.80	4.84
760	11.13	5.54	10.49	5.76	6.65	4.81	4.78	3.04	7.80	4.84
750	11.87	6.05	11.70	6.05	6.77	4.79	4.70	3.21	8.27	5.07
740	11.76	6.10	12.03	6.01	6.75	4.67	4.91	3.19	8.36	5.01

Results are the ensemble means of TKE, ETKE and (ETKE–TKE)/TKE averaged from the three wind turbine parameterizations. Only the data corresponding to daytime MODIS measurements (~10:30, ~13:30) are shown

As the wind farm impact on LST is small in magnitude and is a low-frequency signal, we attempt to isolate this signal from the high-frequency LST variations that are controlled by regional and large-scale weather/climate patterns. The background LSTs are also modified by surface heterogeneity due to spatial differences in land surface properties (e.g., topography, soil moisture, vegetation type/amount) which introduce local LST anomalies as well. Due to solar heating and surface heterogeneity, the MODIS LST shows substantially stronger spatial and temporal variations at daytime than nighttime (Zhou et al. 2012, 2013a). These factors, together with the small ratio of (ETKE–TKE)/TKE will make it difficult to detect and quantify wind farm impacts, particularly at pixel level during the daytime when their effects on the background LST are the strongest.

It is possible that there is a daytime cooling effect over the wind farms as shown in Table 2, but the high-frequency background signal masks the spatial coupling of LST changes with the wind farms (Figs. 3, 4; Table 2). If so, the spatial coupling method we employed may fail to detect such a cooling effect. To address this issue, we explored alternative approaches. For example, we used EOF analysis to decompose the JJA daytime LST in Fig. 3c, d into different spatial patterns; the second EOF mode shows a slightly better signal coupled with the wind farms (figure not shown), but overall this coupling is less convincing than that at nighttime. Our second method (the areal mean ΔLST) may be a better method to quantify the daytime impact as the spatial averaging over the two groups of pixels will smooth the background high-frequency signal. We speculate that at least some of the cooling effects shown in Table 2 could result from the wind farms, but the approaches used have limitations and thus this attribution cannot be asserted with confidence. This may require a different approach or higher resolution data. This will be explored in future work.

As the field observations are only point measurements, the calculated (ETKE–TKE)/TKE ratio represents the relative contribution of the turbine-induced turbulence versus the background TKE for a single wind turbine, whereas the LST changes detected by MODIS account for the collective impact of wind farm-induced mixing

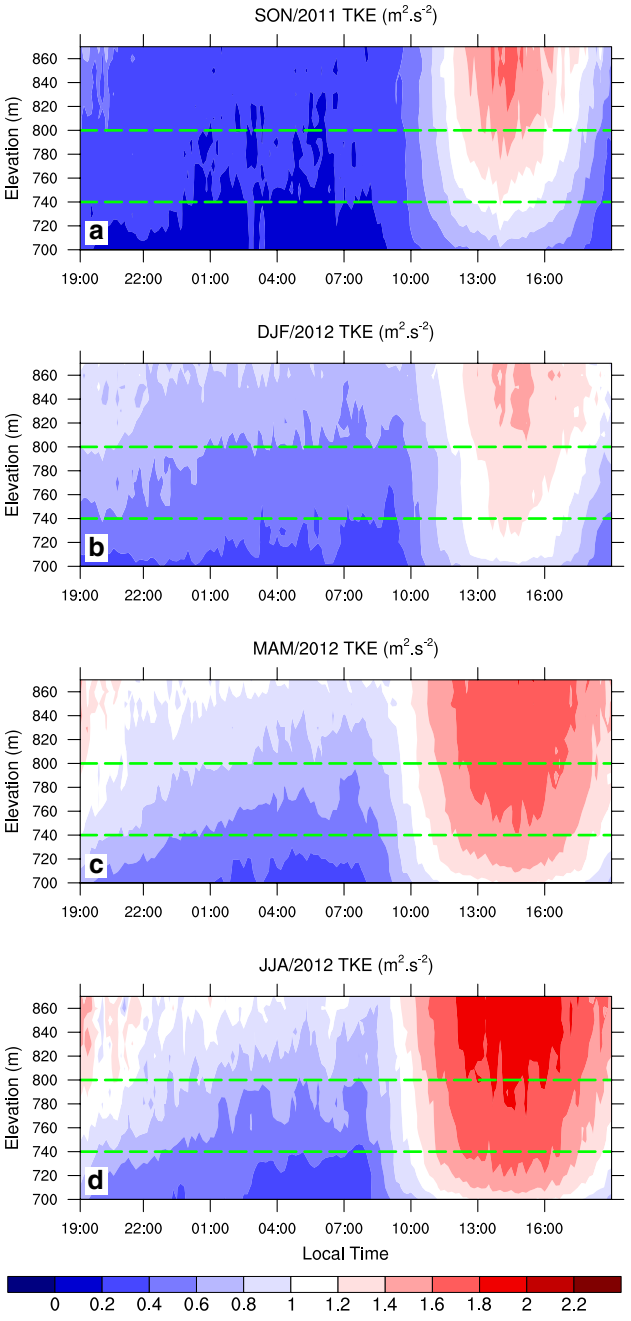

Fig. 8 Seasonal variations in the diurnal cycle of TKE (m^2s^{-2}) measured at Colorado City, TX for the period Sep/2011–Aug/2012: **a** SON/2011, **b** DJF/2012, **c** MAM/2012, and **d** JJA/2012. The *green dashed lines* (740–800 m) indicate the most active layer of turbine-generated turbulence

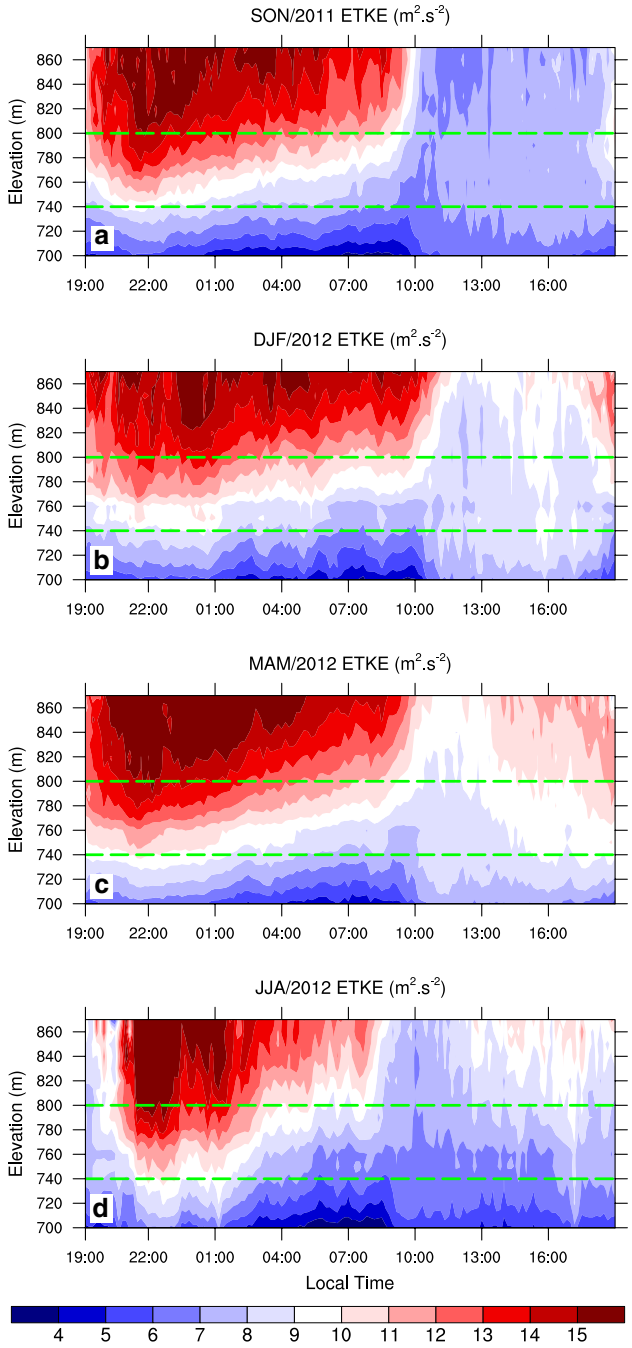

Fig. 9 Same as Fig. 8 but for ETKE

including the wind farm wake effect. Therefore, the ratio might overestimate the mixing at both daytime and nighttime, but the significant diurnal and seasonal variations should still be valid. The ratio generally shows strong correlation with the nighttime LST warming signals over the wind farms. However, as discussed above, exceptions do occur. For instance, the ratio in DJF/2012 is the second largest of the four seasons but the warming signal is the smallest. Other factors such as the strength of the atmospheric inversion should be considered. It is also possible that these exceptions result from uncertainties and gaps in the SODAR and sonic measurements. For example, the DJF/2011 TKE is averaged from 91 days, while the JJA/2012 TKE analysis only had 61 observation days. Most importantly, the field campaign only lasted for 1 year, which is too short to draw confident

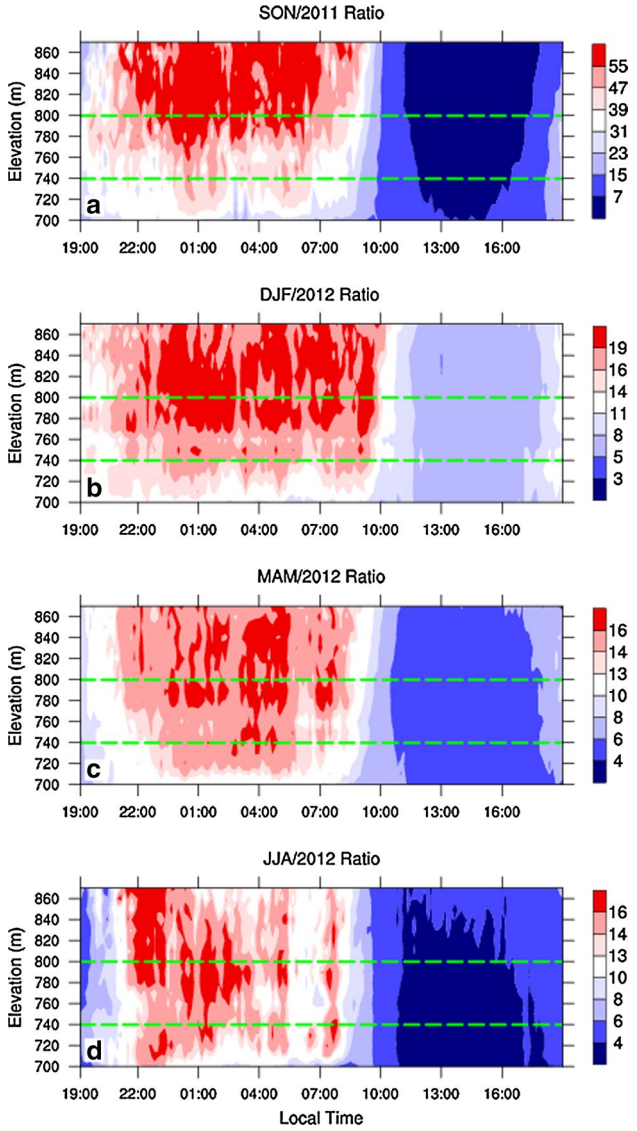

Fig. 10 Same as Fig. 8 but for the ratio of (ETKE–TKE)/TKE

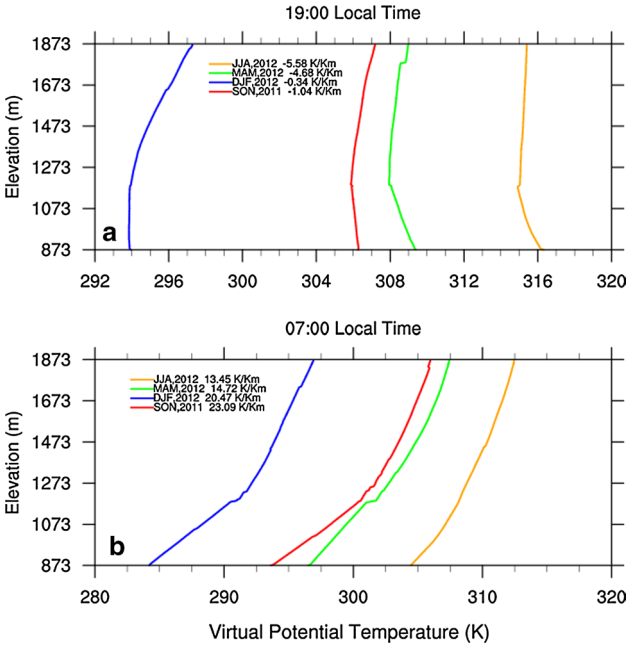

Fig. 11 Seasonal variations of virtual potential temperature profiles measured at Midland, TX (WBAN: 23023; Station height: 873) at **a** 19:00 and **b** 07:00 LT for the period Sep/2011–Aug/2012. The virtual temperature gradients, which are labeled in the figure, are estimated from the lowest 200 m layer (873–1073 m)

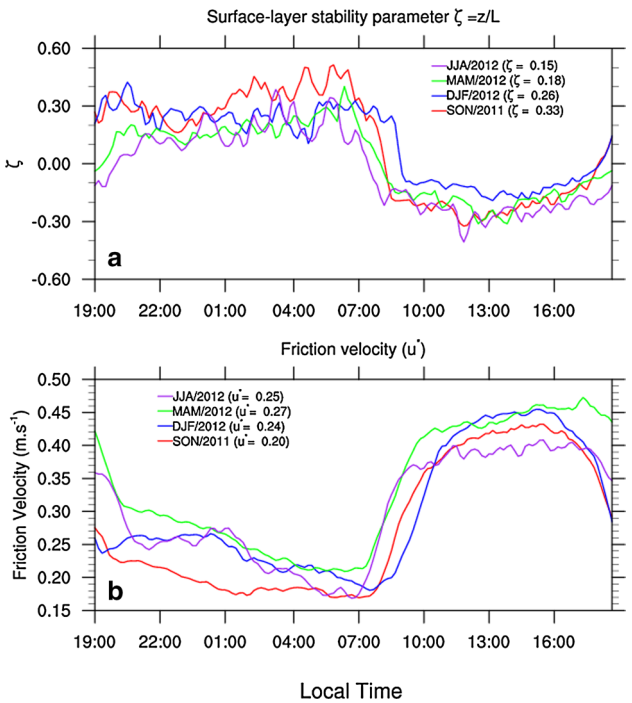

Fig. 12 Seasonal variations in the diurnal cycle of surface-layer stability parameter (ξ) and friction velocity (u^*) measured at the Colorado City, TX for the period Sep/2011–Aug/2012: **a** surface-layer stability parameter and **b** friction velocity. The averaged nighttime values (19:00–07:00) are labeled in the figure and z is the measurement height, which is 3.25 m AGL

conclusions about the seasonal and diurnal variability of wind farm effects. Furthermore, MODIS data also contain uncertainties and noise and are affected by mesoscale and synoptic scale weather systems.

4 Conclusions

Using satellite-derived land surface temperature (LST), Zhou et al. (2012, 2013a) found that there is a nighttime warming signal over four wind farms in central-western Texas and this warming effect is greater in summer than in winter and is stronger at ~22:30 LT than at ~01:30 LT. Based on reanalysis data, Zhou et al. (2013a) attributed the diurnal and seasonal variations in the

wind farm-induced warming effect to those in the magnitude of wind speed. This paper further explores the likely mechanisms controlling the seasonal and diurnal variations of wind farm impacts by examining observed atmospheric profiles from a year-long WFIP field campaign. Using radiosonde, SoDAR data, sonic anemometer measurements, and satellite observations, we find that it is the relative contribution induced by the wind turbine relative to the background TKE that greatly determines the impact of wind farms on LST. The normalized ratio (ETKE–TKE)/TKE explains the day–night contrast of the wind farm impact and most of the magnitude of nighttime LST warming signals between two MODIS measurement times (~22:30 and ~01:30 LT). It also explains seasonal variations in the turbine-induced temperature changes except during DJF/2012. Overall the diurnal and seasonal variations in the turbine-induced turbulence relative to the background value play a dominant role in determining the magnitude of wind farm impacts. In addition, atmospheric stability also matters in determining the sign and strength of the net downward heat transport as well as the magnitude of the background TKE.

Our estimated wind farm impacts on temperature are smaller than those estimated from a small number of field campaigns (Baidya Roy and Traiteur 2010; Rajewski et al. 2013; Smith et al. 2013). Note that the magnitude of the warming effect estimated here represents the grid-averaged value over the entire wind farm aggregates, rather than point measurements from field campaigns. However, the turbine enhanced mixing should be confined mostly to the immediate vicinity of each turbine and hence this warming effect should be much larger if averaged only over the smaller surface area affected by the turbines (Slawsky et al. 2015). Furthermore, the temperature change quantified in this study represents surface skin temperature (Zhou et al. 2012) and it is very likely that much larger surface air temperature changes are expected, given the fact that air is a poor heat conductor in terms of heating the ground surface.

As the analysis is only applied to data from a year-long field campaign, our results cannot explain all of the observed LST changes over the wind farms, particularly some of the seasonal and inter-annual variations in the LST signals. There are uncertainties in the data and in our attribution/detection methods. Other factors, such as the strength of the temperature inversion, should also affect the observed LST changes. Further attribution, however, is limited by the lack of field measurements of atmospheric profiles including wind speed and temperature over the operational wind farms. Although a few short-term field campaigns have observed strong wind farm impacts on near-surface temperature and fluxes, understanding the diurnal evolution of such impacts and relevant process-based mechanisms are lacking. This calls for longer and more comprehensive field campaigns to fully analyze individual and aggregated wind farm impacts, especially the diurnal evolutions of near-surface hydro-meteorology, which may have substantial influences on plant growth, crop productivity, and livestock viability. Although current models such as WRF use simple wind turbine parameterizations that describe relevant ABL-turbine interactions, this study offers a new perspective for understanding turbine-ABL interactions. Examining whether current wind turbine parameterizations can realistically simulate such interactions might provide useful information to validate and improve these parameterizations in weather and climate models.

Wind power is an important part of the solution to climate change, air pollution, and energy problems. Therefore, understanding wind farm impacts on surface–atmosphere exchange processes is critical for developing efficient adaptation and management strategies to ensure long-term sustainability of wind power (Zhou et al. 2013a). The efforts required to identify physical processes of wind turbine-boundary layer interaction are challenging, but the benefits from understanding their effects on weather and climate surely justifies the work invested.

Acknowledgments National Oceanic and Atmospheric Administration (NOAA) and Department of Energy (DOE) are acknowledged for providing the WFIP data. We also would like to thank Jeff Arnfield from NOAA for providing the high-resolution radiosonde data for the period 2012–2013, and three anonymous reviewers for their helpful comments. This work was supported by the National Science Foundation (NSF-AGS-1247137) grant and by the University at Albany Teaching Assistantship.

References

Adams AS, Keith DW (2007) Wind energy and climate: modeling the atmospheric impacts of wind energy turbines. EOS Trans AGU 88 (Fall Meeting Suppl.), abstr. B44B-08

Adams AS, Keith DW (2013) Are global wind power resources estimates overstated? Environ Res Lett. doi:10.1088/1748-9326/8/1/015021

Armstrong A, Waldron S, Whitaker J, Ostle NJ (2014) Wind farm and solar park effects on plant–soil carbon cycling: uncertain impacts of changes in ground-level microclimate. Glob Change Biol. doi:10.1111/gcb.12437

AWEA (2014) U.S. wind industry third quarter 2014 marker report—executive summary. (http://awea.files.cms-plus.com/FileDownloads/pdfs/3Q2014%20AWEA%20Market%20Report%20Public%20Version.pdf)

Baidya Roy S (2011) Simulating impacts of wind farms on local hydrometeorology. J Wind Eng Ind Aerodyn. doi:10.1016/j.jweia.2010.12.013

Baidya Roy S, Traiteur JJ (2010) Impacts of wind farms on surface air temperatures. Proc Natl Acad Sci USA 107:17899–17904

Baidya Roy S, Pacala SW, Walko RL (2004) Can large scale wind farms affect local meteorology? J Geophys Res 109:D19101

Barrie DB, Kirk-Davidoff DB (2010) Weather response to a large wind turbine array. Atmos Chem Phys 10:769–775

Barthelmie RJ (2010) Quantifying the impact of wind turbine wakes on power output at offshore wind farms. J Atmos Ocean Technol 27:1302–1317

Cervarich M, Baidya RS, Zhou L (2013) Spatiotemporal structure of wind farm-atmospheric boundary layer interactions. Energy Procedia 40:530–536

Fitch A, Olson J, Lundquist J, Dudhia J, Gupta A, Michalakes J, Barstad I (2012) Local and mesoscale impacts of wind farms as parameterized in a mesoscale NWP model. Mon Weather Rev 140:3017–3038

Freedman J, Flores I, Zack J, Schroeder J, Ancell B, Brewster K, Basu S, Banunarayanan V, Ela E (2014) The wind forecast improvement project (WFIP): a public/private partnership for improving short term wind energy forecasts and quantifying the benefits of utility operations—the southern study area

Harris RA, Zhou L, Xia G (2014) Satellite observations of wind farm impacts on nocturnal land surface temperature in Iowa. Remote Sens 6(12):12234–12246

Keith D, DeCarolis J, Denkenberger D, Lenschow D, Malyshev S, Pacala S, Rasch PJ (2004) The influence of large-scale windpower on global climate. Proc Natl Acad Sci USA 101:16115–16120

Kirk-Davidoff DB, Keith DW (2008) On the climate impact of surface roughness anomalies. J Atmos Sci 65:2215–2234

Obukhov AM (1946) Turbulence in an atmosphere with a non-uniform temperature. Bound Layer Meteorol 2:7–29

Petersen EL, Mortensen NG, Landberg L, Højstrup J, Frank HP (1997) Wind power meteorology. Risø National Laboratory, Roskilde

Rajewski D, Tackle E, Lundquist J, Oncley S, Prueger J, Horst T, Rhodes M, Pfeiffer R, Hatfield J, Spoth K, Doorenbos R (2013) Crop wind energy experiment (CWEX): observations of surface-layer, boundary layer, and mesoscale interactions with a wind farm. Bull Am Meteorol Soc 94:655–672

Rhodes ME, Lundquist JK (2013) The effect of wind-turbine wakes on summertime US midwest atmospheric wind profiles as observed with ground-based Doppler lidar. Bound Layer Meteorol 149:85–103

Seidel DJ, Ao CO, Li K (2010) Estimating climatological planetary boundary layer heights from radiosonde observations: comparison of methods and uncertainty analysis. J Geophys Res 115:D16113. doi:10.1029/2009JD013680

Slawsky L, Zhou L, Baidya RS, Xia G, Vuille M, Harris RA (2015) Observed thermal impacts of wind farms over northern illinois. Sensors (under revision)

Smith CR, Barthelmie RJ, Pryor SC (2013) In situ observations of the influence of a large onshore wind farm on near-surface temperature, turbulence intensity and wind speed profiles. Environ Res Lett 8:034006

Stull RB (1988) An introduction to boundary layer meteorology, vol 13. Springer, New York

Wan Z (2002) Estimate of noise and systematic error in early thermal infrared data of the moderate resolution imaging spectroradiometer (MODIS). Remote Sens Environ 80:47–54

Wan Z (2006) New refinements and validation of the MODIS land surface temperature/emissivity products. Remote Sens Environ 112:59–74

Wang C, Prinn RJ (2010) Potential climatic impacts and reliability of very large scale wind farms. Atmos Chem Phys 10:2053–2061

Wilczak J, Finley C, Freedman J, Cline J, Bianco L, Olson J, Djalalova I, Sheridan L, Ahlstrom M, Manobianco J, Zack J, Carley J, Benjamin S, Marquis M (2014) The wind forecast improvement project (WFIP): a public-private partnership addressing wind energy forecast needs. Bull Am Meteorol Soc. doi:10.1175/BAMS-D-14-00107.1

Zhou L, Tian Y, Baidya Roy S, Thorncroft C, Bosart LF, Hu Y (2012) Impacts of wind farms on land surface temperature. Nat Clim Chang 2(7):539–543

Zhou L, Tian Y, Baidya RS, Dai Y, Chen H (2013a) Diurnal and seasonal variations of wind farm impacts on land surface temperature over western Texas. Clim Dyn 41:307–326

Zhou L, Tian Y, Chen H, Dai Y, Harris RA (2013b) Effects of topography on assessing wind farm impacts using MODIS data. Earth Interact 17(13):1–18